

Porous Pt–M (M = Cu, Zn, Ni) nanoparticles as robust nanocatalysts†

Si-Bo Wang,[‡] Wei Zhu,[‡] Jun Ke, Jun Gu, An-Xiang Yin, Ya-Wen Zhang* and Chun-Hua Yan*

Cite this: *Chem. Commun.*, 2013, **49**, 7168

Received 1st May 2013,
Accepted 15th June 2013

DOI: 10.1039/c3cc43208d

www.rsc.org/chemcomm

Porous Pt–M (M = Cu, Zn, Ni) nanoparticles (NPs) were obtained by reduction of [Pt(CH₃NH₂)₄][PtCl₄] and M(Ac)₂ (or MCl₂) with oleylamine under mild conditions. The porous Pt–Cu NPs exhibited superior catalytic activities over a Pt/Cu NP mixture and Cu NPs as references for CO oxidation processes.

Metal nanoparticles (NPs) are currently the frontier subject of vigorous research because of their unique properties and wide applications in catalysis,¹ sensors,² biological imaging,³ photothermal therapy,⁴ and surface-enhanced Raman scattering.⁵ In these research studies, the morphology or shape of metal NPs has been demonstrated to directly influence their material performances for the alternations in facets (or surface structure), electronic structure, surface bonding with ligands, and assembly patterns of the NPs.^{1–6} Among the shape tunable nanomaterials, porous ones, such as nanoboxes,⁷ nanocages,⁸ spherical nanoshells,⁹ and hollow nanocrystals with faceted shape,¹⁰ are applied in optical sensing,¹¹ catalysis,¹² and drug delivery.¹³

Pt nanomaterials have been widely utilized as active components in heterogeneous catalytic processes, such as oxygen reduction in fuel cells¹ and NO_x selective reduction.¹⁴ In order to obtain robust Pt based nanocatalysts with maximized catalytic performances as well as minimized Pt consumption, great efforts have been made in the controllable synthesis and nanostructure optimization of Pt based bi- or trimetallic nanostructures by adopting non-precious transition metals, including Pt–Ni,¹⁵ Pt–Co,¹⁶ Pt–Cu,¹⁷ Pt–Sn,¹⁸ and Pt–Zn.¹⁹ More recently, Lou's group reported that cubic PtCu₃ nanocages prepared by a solvothermal method exhibited high catalytic activity for methanol electro-oxidation processes.²⁰ So far, most solution approaches to obtain porous metal nanostructures consisted of two steps: firstly forming solid NPs and then making voids through the

Kirkendall effect or galvanic replacement, pitting, etching, and dealloying corrosion.^{7–13,20}

Herein, we report a general one-pot synthesis of porous Pt–M (M = Cu, Ni, Zn) NPs with high shape selectivities. The porous Pt–Cu NPs (supported on commercial TiO₂) showed considerably enhanced catalytic activity for CO oxidation with respect to the Pt/Cu NP mixture and Cu NPs.

In a typical synthesis of porous Pt–Cu NPs, methyl substituted magnus' green salt (MSMGS, 5 mg, 16.7 μmol), cupric acetate monohydrate (Cu(Ac)₂·H₂O, 3.3 mg, 16.7 μmol) and purified oleylamine (OAm, 8.1 g) were mixed in a glass colorimetric tube (10 mL), and then, the tube with a sealed stopper was kept in an electric oven at 140 °C for one week.

Analyses by means of both energy-dispersive X-ray spectroscopy (EDS) and inductively coupled plasma-atomic emission spectrometry (ICP-AES) showed that the ratio of Pt : M was about 1 : 4 for Pt–Cu NPs (Pt_{0.2}Cu_{0.8}), 9 : 1 for Pt–Zn NPs (Pt_{0.9}Zn_{0.1}), and 6 : 4 for Pt–Ni NPs (Pt_{0.6}Ni_{0.4}) (Table S1, ESI†). As shown in the transmission electron microscopy (TEM) image in Fig. 1a, the Pt_{0.2}Cu_{0.8} NPs were obtained with a narrow size distribution (18.5 ± 1.0 nm in size, Fig. S1a, ESI†). As illustrated in the high-resolution TEM (HRTEM) image (Fig. S2a, ESI†), the sharp contrast but blurring lattice fringes observed for one single particle explicitly indicated that the Pt_{0.2}Cu_{0.8} NPs have a semi-crystalline cage-like porous structure, similar to those of the PtCu₃ frameworks fabricated by Lou and his coworkers.²⁰ According to the high angle annular dark field scanning transmission electron microscopy (HAADF-STEM) images (Fig. S3, ESI†) and HAADF-STEM-EDS line scan profiles, the Pt_{0.2}Cu_{0.8} NPs exhibited a partially segregated structure, instead of an ideal alloy structure (Fig. 1b). The powder X-ray diffraction (PXRD) pattern of the Pt_{0.2}Cu_{0.8} NPs (Fig. S4, ESI†) was assignable to fcc structured Cu with a slight shift to low angle due to the lattice expansion from the doping of a small amount of Pt into Cu. This lattice expansion also coincided well with the observation from the HRTEM image (Fig. S2a, ESI†). As shown in panels c and d of Fig. 1, the as-prepared Pt_{0.9}Zn_{0.1} and Pt_{0.6}Ni_{0.4} NPs showed dendritic porous structures of sizes 26.8 ± 2.4 nm, and 16.2 ± 1.6 nm, respectively (Fig. S1b and c, ESI†). As judged from the HAADF-STEM-EDS line scan profiles (Fig. S5, ESI†) and PXRD patterns (Fig. S4, ESI†), the Pt_{0.9}Zn_{0.1} and Pt_{0.6}Ni_{0.4} NPs probably took an fcc alloy structure with less

Beijing National Laboratory for Molecular Sciences, State Key Laboratory of Rare Earth Materials Chemistry and Applications, PKU-HKU Joint Laboratory in Rare Earth Materials and Bioinorganic Chemistry, and College of Chemistry and Molecular Engineering, Peking University, Beijing 100871, China.

E-mail: ywzhang@pku.edu.cn, yan@pku.edu.cn; Fax: +86-10-62756787

† Electronic supplementary information (ESI) available: Synthesis details, more TEM images, instrumental characterization, and catalysis results. See DOI: 10.1039/c3cc43208d

‡ These authors contributed equally.

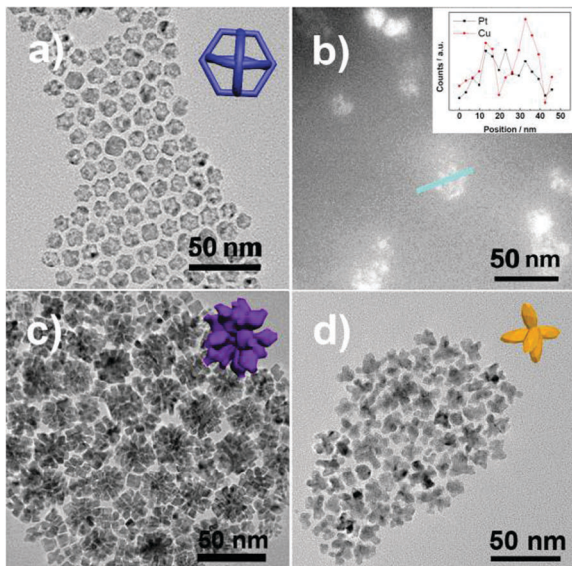


Fig. 1 (a) TEM image (inset: geometry model) and (b) HADDF-STEM-EDS line-scan profile of the Pt–Cu NPs. TEM images (insets: geometry models) of the (c) Pt–Zn and (d) the Pt–Ni NPs.

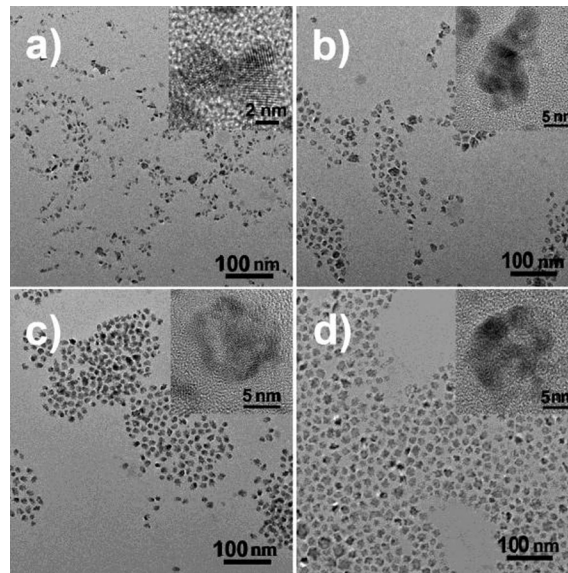


Fig. 2 TEM images of the Pt–Cu NPs taken at different reaction times: (a) 12 h, (b) 1 day, (c) 2 days, and (d) 5 days.

segregations. From Scherrer analysis of (111) peaks of these NPs in the PXRD pattern, the crystalline domain sizes of $\text{Pt}_{0.2}\text{Cu}_{0.8}$, $\text{Pt}_{0.9}\text{Zn}_{0.1}$ and $\text{Pt}_{0.6}\text{Ni}_{0.4}$ NPs were calculated to be 6.0, 18.6, and 6.7 nm, respectively. The $\text{Pt}_{0.9}\text{Zn}_{0.1}$ and $\text{Pt}_{0.2}\text{Cu}_{0.8}$ NPs showed higher crystallinity than the $\text{Pt}_{0.6}\text{Ni}_{0.4}$ NPs (Fig. S2b, c and S4, ESI[†]).

Experimentally, $\text{Cu}(\text{Ac})_2$ appeared to be well dispersed in OAm while MSMGS was insoluble in it.²¹ Upon further considering $\text{Pt}(\text{II})$ ($\varphi^\circ([\text{PtCl}_4]^{2-}/\text{Pt}) = 0.758 \text{ V}$) showing a higher affinity to the amine group of OAm than $\text{Cu}(\text{II})$ ($\varphi^\circ(\text{Cu}^{2+}/\text{Cu}) = 0.340 \text{ V}$), it seemed to be easier to reduce $\text{Cu}(\text{Ac})_2$ than MSMGS in OAm. However, $\text{Ni}(\text{II})$ ($\varphi^\circ(\text{Ni}^{2+}/\text{Ni}) = -0.257 \text{ V}$) and $\text{Zn}(\text{II})$ ($\varphi^\circ(\text{Zn}^{2+}/\text{Zn}) = -0.762 \text{ V}$) possessed weak reducibility in this case. Thus, the final Pt/M ratios in Pt–Zn and Pt–Ni NPs were higher than those in Pt–Cu NPs, and the phase distinction between hcp Zn and fcc Pt might further reduce the Zn content in the Pt–Zn NPs during the alloying process.

Time-sequential TEM (Fig. 2) and ICP-AES analyses (Fig. S6, ESI[†]) were carried out to reveal the possible growth stages of the porous Pt–Cu NPs. During the synthesis, the solution turned brown after 8 h of heating, indicating the start of the reduction of both MSMGS and $\text{Cu}(\text{Ac})_2$ by OAm. Moreover, small twinned NPs formed after 12 h of reaction (Fig. 2a) and turned into irregular porous NPs during concurrent growth in the first two days (Fig. 2b and c). The defect sites on the twinned seeds might guide the Pt–Cu NPs to grow anisotropically. For the formed Pt–Cu NPs, the Cu/Pt ratio increased suddenly from 45 : 55 at 12 h to 73 : 23 at one day, and slowly increased up to 80 : 20 from 1 day to 5 days (Fig. S6, ESI[†]). Although $\text{Pt}(\text{II})$ had a higher standard electrode potential than $\text{Cu}(\text{II})$, the insolubility of the $\text{Pt}(\text{II})$ precursor and the strong affinity of the $-\text{NH}_2$ group to $\text{Pt}(\text{II})$ retarded the reduction of $\text{Pt}(\text{II})$. Afterwards, the shape of the NPs became uniform, and their sizes and compositions changed little (Fig. 1a and 2d; Fig. S6, ESI[†]) from 5 days to one week. However, the NPs obtained from two-week reaction became polydispersed (Fig. S7, ESI[†]).

The effects of the other reaction parameters on this synthesis were also investigated. As the $\text{Cu}(\text{II})/\text{Pt}(\text{II})$ ratio increased, the size of the NPs augmented (Fig. S8, ESI[†]). Given that the amount of the Pt precursor

did not change, which possibly gave rise to the same morphology and quantity of seeds, the amount of the Cu precursor determined the eventual size of the NPs. In addition, Cu precursors gradually dominated the final morphology with the increasing amount. Poly-dispersed irregular NPs of larger size were finally obtained at high $\text{Cu}(\text{II})/\text{Pt}(\text{II})$ ratios (Fig. S8d–f, ESI[†]). Meanwhile, only nanoicosahedrons and imperfect triangle nanoplates were acquired by the reduction of the Pt precursor (Fig. S8a, ESI[†]). Therefore, a suitable $\text{Cu}(\text{II})/\text{Pt}(\text{II})$ ratio (1 : 1) was essential for this synthesis. Temperature (T) was another significant factor. Higher T yielded better crystallized NPs with more smooth surfaces (Fig. S9 and S10, ESI[†]), while lower T led to more small particles and more rough surfaces to big NPs.

If K_2PtCl_4 , $[\text{Pt}(\text{ethylenediamine})_2][\text{PtCl}_4]$, or $\text{Pt}(\text{acac})_2$ was used to replace MSMGS in the synthesis, similar cage-like Pt–Cu structures could not be obtained (Fig. S11a–c, ESI[†]). Upon further considering the linear structure of MSMGS, the unique metal–metal chain might decrease the reduction potential of $\text{Pt}(\text{II})$,²¹ which postponed the reduction of the Pt precursor, and thus facilitated the hollowing process of the NPs. This suggests that the special structure of MSMGS was probably a prerequisite for the preparation of porous Pt–Cu NPs. However, in the presence of MSMGS, either using $\text{Cu}(\text{Ac})_2$ or CuCl_2 as a Cu precursor, similar cage-like $\text{Pt}_{0.2}\text{Cu}_{0.8}$ NPs (Fig. S11d, ESI[†]) were formed, indicating that the anion species of cupric salts did not affect the formation of porous Pt–Cu NPs.

Upon using MSMGS and $\text{Cu}(\text{Ac})_2$ as precursors for reactions at 140°C for one week, as the amount of the precursors increased, the reaction rate seemed to considerably increase,²¹ and the NPs became bigger and more smooth (Fig. S12, ESI[†]). In this case, a more thermodynamically favoured structure processing smooth surfaces was formed for the NPs. Hence, such a metastable porous structure with rough surfaces can be obtained under mild reaction conditions.

Different from the porous multi-metallic nanostructures obtained using the normal formation process (which was usually a subsequent galvanic etching process²²), the as-obtained Pt–Cu NPs became porous from the start of the synthetic reaction.

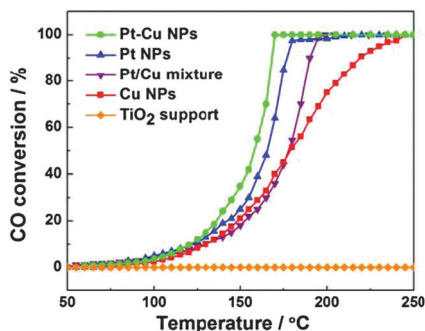


Fig. 3 CO conversion percentage versus reaction temperature for the NPs loaded onto a commercial TiO₂ support (0.2 wt%, both Pt and Cu included).

Firstly, the reduction of Cu(II) and Pt(II) occurred simultaneously with formation of small multiply twinned Pt-Cu NPs (Fig. 2a). Then, such small NPs formed porous structures *via* the coalescence between each other. The size of Pt-Cu NPs stopped increasing while the hollow structures were formed after two days' reaction (Fig. 2c). And the Cu/Pt ratio of the NPs stopped increasing (Fig. S6, ESI[†]). Finally, the porous structures were obtained with a narrow size distribution (Fig. 1a and 2d).

The formation of the porous Pt-M structure was possibly due to the generation of defective twinned seeds at the start of the reaction and the concurrent anisotropic growth limited by insufficient mass diffusion of metal atoms, directed by the twin defects under the combined action of the galvanic replacement between Pt(II) in solution and surface M(0) atoms of the NPs, and the Kirkendall effect.^{20,22} The galvanic reaction would cause strong mass diffusion disturbance during the alloying of Pt with M to create pores, and the existence of the Kirkendall effect would make the Pt-Cu NPs undergo an internal diffusion procedure at defect sites during the coalescence of NPs due to the ease of forming Pt-Cu alloys.^{20,23} As a result, cage-like porous structure was created for the Pt-Cu NPs. However, Ni has a much lower heat of mixing in Pt-M than Cu,²³ indicating a retarded alloying process for Pt-Ni. Further, the alloying of Pt with Zn seems to be more difficult than that with Cu probably due to their different crystal structures.^{19,20,23} Thus, the hollowing process due to galvanic reaction and/or the Kirkendall effect was restrained for Pt-Ni and Pt-Zn NPs for their obviously retarded alloying reaction. In this case, dendritic Pt-Zn and Pt-Ni NPs formed due to the coalescing of the NPs from the defective seeds, as confirmed by the single-crystalline nature of the NPs revealed by the HRTEM images (Fig. S2b and c, ESI[†]).

The catalytic activity of the Pt_{0.2}Cu_{0.8} NPs on TiO₂ (Fig. S13, ESI[†]) was tested for CO oxidation processes (Fig. 3). After ruling out the effect of surfactant residuals after calcination (Fig. S14, ESI[†]) on this measurement, Pt and Cu NPs prepared using similar methods were used as the references (ESI[†]). The porous Pt-Cu NPs had a much higher surface area than Pt NPs and Cu NPs (Table S2, ESI[†]). Fig. S13 showed that the porous Pt-Cu NPs could be well immobilized on TiO₂ before and after calcination, but took upon partial collapse of pores along with a slight size decrease after annealing. Compared with Pt NPs (composed of 18.5 nm icosahedrons and 41.2 nm triangular planes; Fig. S8a, ESI[†]; S_{BET} : 6.6 m² g⁻¹), Cu NPs (*ca.* 94 nm; Fig. S8f, ESI[†]; S_{BET} : 4.7 m² g⁻¹) and a mixture of Pt and Cu NPs, the porous Pt_{0.2}Cu_{0.8} NPs (S_{BET} : 260 m² g⁻¹) had the highest catalytic activity as illustrated in Fig. 3. Compared to Pt NPs (light-off temperature, T_{50} = 166 °C), the

Pt_{0.2}Cu_{0.8} NPs (T_{50} = 158 °C) exhibited similar activity towards CO oxidation, but with the reduction of Pt content to a quarter. This may have possibly resulted from the exposure of more accessible Pt active sites in the porous structure associated with the high surface area of the hollow NPs. A stability test showed that no obvious activity degeneration was observed for the Pt_{0.2}Cu_{0.8} NPs in five catalytic cycles (Fig. S15, ESI[†]), probably because well immobilization of the NPs on TiO₂ could stabilize the structure and composition of the catalysts and thus the catalytic activity (Fig. S13, ESI[†]).²⁴ A further catalytic test showed that the porous Pt-Cu NPs were also active for preferential CO oxidation (PROX) reactions, attaining a maximum activity (42% CO conversion) at 160 °C, and a high selectivity (90% in O₂ converted to CO₂ to the total O₂ consumed) at 110 °C (Fig. S16, ESI[†]).

To sum up, we developed a one-step solution approach towards cage-like porous Pt-Cu NPs and dendritic porous Pt-Zn, Pt-Ni NPs under mild reaction conditions. The hollow Pt-Cu NPs were active for both CO oxidation and PROX reactions, indicating that they are promising nanocatalysts for applications.

This work was supported by the NSFC (Grant No. 21025101 and 21271011). Y.W.Z. particularly appreciates the financial aid of China National Funds for Distinguished Young Scientists from the NSFC.

Notes and references

- 1 B. Lim, M. J. Jiang, P. H. C. Camargo, E. C. Cho, J. Tao, X. M. Lu, Y. M. Zhu and Y. N. Xia, *Science*, 2009, **324**, 1302.
- 2 E. M. Larsson, J. Alegret, M. Kall and D. S. Sutherland, *Nano Lett.*, 2007, **7**, 1256.
- 3 A. P. Alivisatos, *Nat. Biotechnol.*, 2004, **22**, 47.
- 4 X. H. Huang, I. H. El-Sayed, W. Qian and M. A. El-Sayed, *J. Am. Chem. Soc.*, 2006, **128**, 2115.
- 5 M. J. Mulvihill, X. Y. Ling, J. Henzie and P. D. Yang, *J. Am. Chem. Soc.*, 2010, **132**, 268.
- 6 K. B. Zhou and Y. D. Li, *Angew. Chem., Int. Ed.*, 2012, **51**, 602.
- 7 J. Zeng, Q. Zhang, J. Y. Chen and Y. N. Xia, *Nano Lett.*, 2010, **10**, 30.
- 8 Y. Yamauchi, A. Sugiyama, R. Morimoto, A. Takai and K. Kuroda, *Angew. Chem., Int. Ed.*, 2008, **47**, 5371.
- 9 B. G. Prevo, S. A. Esakoff, A. Mikhailovsky and J. A. Zasadzinski, *Small*, 2008, **4**, 1183.
- 10 Y. D. Yin, C. Erdonmez, S. Aloni and A. P. Alivisatos, *J. Am. Chem. Soc.*, 2006, **128**, 12671.
- 11 A. M. Schwartzberg, T. Y. Olson, C. E. Talley and J. Z. Zhang, *J. Phys. Chem. B*, 2006, **110**, 19935.
- 12 Y. Wu, D. S. Wang, Z. Q. Niu, P. C. Chen, G. Zhou and Y. D. Li, *Angew. Chem., Int. Ed.*, 2012, **51**, 12524.
- 13 M. S. Yavuz, Y. Y. Cheng, J. Y. Chen, C. M. Cobley, Q. Zhang, M. Rycenga, J. W. Xie, C. Kim, K. H. Song, A. G. Schwartz, L. V. Wang and Y. N. Xia, *Nat. Mater.*, 2009, **8**, 935.
- 14 S. H. Zhou, B. Varughese, B. Eichhorn, G. Jackson and K. Mellwrath, *Angew. Chem., Int. Ed.*, 2005, **44**, 4539.
- 15 V. R. Stamenkovic, B. Fowler, B. S. Mun, G. F. Wang, P. N. Ross, C. A. Lucas and N. M. Markovic, *Science*, 2007, **315**, 493.
- 16 V. R. Stamenkovic, B. S. Mun, M. Arenz, K. J. J. Mayrhofer, C. A. Lucas, G. F. Wang, P. N. Ross and N. M. Markovic, *Nat. Mater.*, 2007, **6**, 241.
- 17 P. Strasser, S. Koh, T. Anniyev, J. Greeley, K. More, C. F. Yu, Z. C. Liu, S. Kaya, D. Nordlund, H. Ogasawara, M. F. Toney and A. Nilsson, *Nat. Chem.*, 2010, **2**, 454.
- 18 Y. Liu, D. G. Li, V. R. Stamenkovic, S. Soled, J. D. Henao and S. H. Sun, *ACS Catal.*, 2011, **1**, 1719.
- 19 Y. J. Kang, J. B. Pyo, X. C. Ye, T. R. Gordon and C. B. Murray, *ACS Nano*, 2012, **6**, 5642.
- 20 B. Y. Xia, H. B. Wu, X. Wang and X. W. Lou, *J. Am. Chem. Soc.*, 2012, **134**, 13934.
- 21 W. Zhu, A. X. Yin, Y. W. Zhang and C. H. Yan, *Chem.-Eur. J.*, 2012, **18**, 12222.
- 22 E. Gornzalez, J. Arbiol and V. F. Puntes, *Science*, 2011, **334**, 1377.
- 23 S. M. Foiles, M. I. Baskin and M. S. Daw, *Phys. Rev. B*, 1986, **33**, 7983.
- 24 N. N. Hoover, B. J. Auten and B. D. Chandler, *J. Phys. Chem. B*, 2006, **110**, 8606.